

Cloud removal in remote sensing images using generative adversarial networks and SAR-to-optical image translation

Faramarz Naderi Darbaghshahi^a, Mohammad Reza Mohammadi^a, Mohsen Soryani^{a,*}

^a*School of Computer Engineering, Iran University of Science and Technology
University Road, Hengam Street, Resalat Square, Narmak, Tehran, P.O. Box 16846-13114, Iran*

Abstract

Satellite images are often contaminated by clouds. Cloud removal has received much attention due to the wide range of satellite image applications. As the clouds thicken, the process of removing the clouds becomes more challenging. In such cases, using auxiliary images such as near-infrared or synthetic aperture radar (SAR) for reconstructing is common. In this study, we attempt to solve the problem using two generative adversarial networks (GANs). The first translates SAR images into optical images, and the second removes clouds using the translated images of prior GAN. Also, we propose dilated residual inception blocks (DRIBs) instead of vanilla U-net in the generator networks and use structural similarity index measure (SSIM) in addition to the L1 Loss function. Reducing the number of downsamplings and expanding receptive fields by dilated convolutions increase the quality of output images. We used the SEN1-2 dataset to train and test both GANs, and we made cloudy images by adding synthetic clouds to optical images. The restored images are evaluated with PSNR and SSIM. We compare the proposed method with state-of-the-art deep learning models and achieve more accurate results in both SAR-to-optical translation and cloud removal parts.

Keywords: Cloud Removal, SAR-to-optical translation, Generative Adversarial Network (GAN), Deep Learning, SAR, Optical Imagery

1. Introduction

Remote sensing plays a vital role in acquiring information for monitoring various fields such as recognizing buildings (Vakalopoulou et al., 2015), crop mapping (Kussul et al., 2017), and land cover change detection (Lyu et al., 2016). A study was conducted by Moderate Resolution Imaging Spectroradiometer (MODIS) over 12 years of continuous observations from Terra and over nine years from Aqua showed that clouds cover around 67% of the Earth's surface (King et al., 2013). Therefore, cloud removal methods are considered to address this issue in optical remote sensing.

There are four categories for reconstructing the missing information on remote sensing data (Shen et al., 2015): (1) spatial-based methods; (2) spectral-based methods; (3) temporal-

*Corresponding author

Email addresses: `f_naderi97@comp.iust.ac.ir` (Faramarz Naderi Darbaghshahi),
`mrmohammadi@iust.ac.ir` (Mohammad Reza Mohammadi), `soryani@iust.ac.ir` (Mohsen Soryani)

based methods; and (4) hybrid methods. Since clouds cause missing information, we can use these methods for cloud removal.

Spatial-based methods restore corrupted pixels using cloud-free regions. Maalouf et al. (2009) use bandelet transform and the multiscale geometrical grouping. Meng et al. (2017) present an adaptive patch method based on a sparse dictionary learning algorithm. These methods usually fail to recover contaminated pixels if cloud regions are large (Shen et al., 2015).

Spectral-based methods use different sensors to acquire additional data for reconstructing missing information. The auxiliary data can be obtained by optical sensors (Zhang et al., 2018), but they also can be contaminated by clouds. To solve this problem, additional sources must be able to pass-through clouds, e.g., near-infrared (Enomoto et al., 2017; Wang et al., 2005) or SAR (Gao et al., 2020; Li et al., 2019; Meraner et al., 2020).

Temporal-based methods estimate missing information by integrating cloud-free correspondence images at different times. Chen et al. (2019) present an end-to-end deep learning architecture to detect and remove clouds from high-resolution satellite data. Xu et al. (2016) remove clouds with combined coefficients from the reference image (cloud-free areas) and the dictionary learned from the target image (cloudy areas). Requiring cloud-free images with short intervals is the limitation of these methods.

Hybrid methods utilize a combination of the three previous methods for cloud removal. Cheng et al. (2014) find the most suitable pixel for the corrupted area with a spatio-temporal Markov random field (MRF) model. Zhang et al. (2020) fill cloudy regions by a spatio-temporal patch group deep learning framework. Benabdelkader et al. (2007) improve the contextual reconstruction process with spatio-spectral information.

SAR images are widely used in cloud removal because of their advantages, such as passing through clouds and smoke. They can be obtained 24 hours a day and regardless of the weather conditions. However, disadvantages such as speckle noise, lack of color information, and geometry distortion and shadows cause experts unable to distinguish between different areas. Using SAR-to-optical translated images is a way to solve this problem (Wang et al., 2019).

Deep learning is a powerful tool to find hidden structures in large data sets by the self feature extracting (LeCun et al., 2015). In recent years, it has improved the performance of remote sensing image analysis tasks such as scene classification, object detection, and land use and land cover (LULC) classification (Ma et al., 2019). Generative Adversarial Networks (GANs) (Goodfellow et al., 2014) have seen a massive rise in popularity among deep learning methods because of their results, especially in the image-to-image translation tasks such as pix2pix (Isola et al., 2017) and Cycle-Consistent Adversarial Networks (CycleGAN) (Zhu et al., 2017). To generate fake images similar to real images, Mirza and Osindero (2014) introduced conditional generative adversarial network (cGAN) by assigning latent space elements to particular data distribution. Bermudez et al. (2019) used cGAN for SAR-to-optical translation with SAR/optical multitemporal data. Singh and Komodakis (2018) trained a CycleGAN to remove clouds.

Based on the aforementioned studies, we introduce a model to cloud removal in remote sensing images using GANs. The main contributions of this work are summarized as follows:

1. Our model includes two GANs. We train the former to discover the intricate structures

in SAR images with large datasets. The latter is used to remove clouds and retains the quality of cloud-free areas.

2. We propose DRIBs for generators based on dilated convolutions to increase receptive view (global view) and prevent missing information.
3. We train and test our model with the SEN1-2 dataset and compare it with state-of-the-art deep learning-based cloud removal methods. The results show the superiority of our model in both SAR-to-optical and cloud removal tasks.

The rest of this paper is structured as follows. In Section 2, the proposed method is explained. The comparison results are presented in Section 3. Also, we show the influence of the SAR-to-optical step, DRIBs, and SSIM loss function in the ablation study. Section 4 provides a discussion on the results, and a conclusion is given in Section 5.

2. Methods

Unlike thin clouds, thick clouds completely block surface information, and we have no information about the areas below the cloud. SAR images help us as auxiliary images for restoring cloudy regions because of their ability to cross the cloud. Translating SAR images to synthetic optical images instead of using SAR images directly to remove the clouds can improve the quality of output images (Wang et al., 2019). The success of GANs in image translation has led us to use them in our method. We use two GANs for the following reasons: (1) The cost of obtaining a large-scale dataset of SAR and optical pair images is less than acquiring co-registered optical cloudy, cloud-free, and SAR images. (2) The training of SAR-to-optical image translation needs many images. As shown in Fig. 1, our method consists of two parts: translation of SAR to optical images and removing clouds. This separation of tasks improves the training phase of SAR-to-optical translation GAN with many available images, and the limitation of the number of co-registered cloudy and cloud-free images does not affect it.

2.1. Network Architecture

For both GANs, we propose the encoder-DRIBs-decoder structure in the generator, as shown in Fig. 2. We adopt symmetrical concatenations between encoder and decoder for giving local information to upsampled outputs (Ronneberger et al., 2015). The details of generator and discriminator networks are presented in Table 1. Table 2 shows DRIB architecture, which we used 8 of it as a bottleneck.

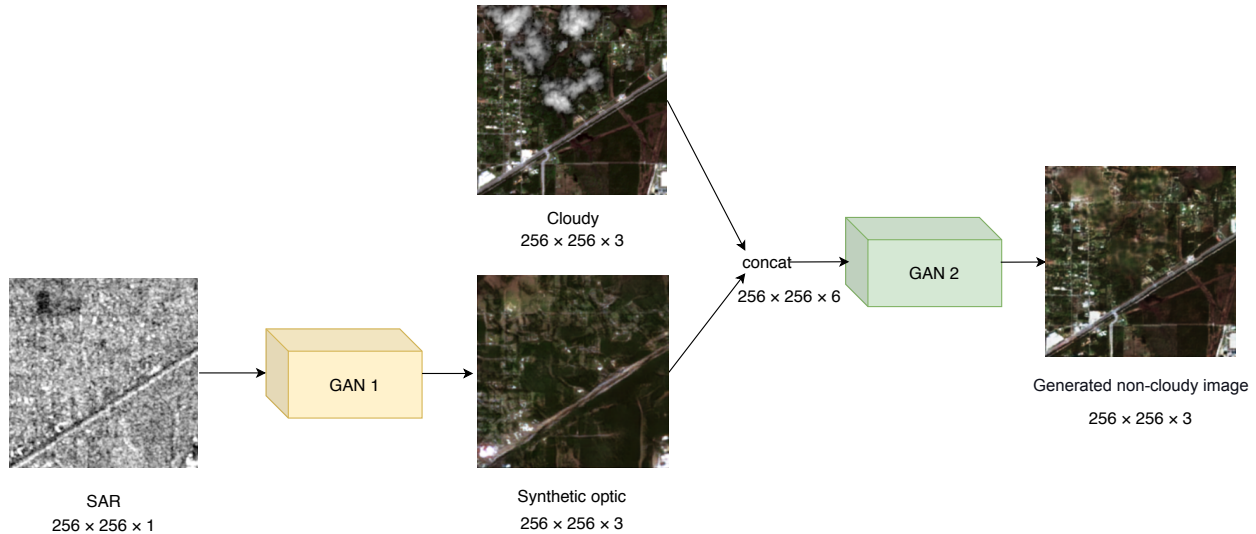


Figure 1: Overview of the model. The tasks of GAN1 and GAN2 include SAR-to-optical translation and cloud removal, respectively.

Table 1: Details of discriminator and generator except DRIBs. Information flow is from top to bottom within components. Acronyms: C=convolution, B=batch normalization, L= leaky relu, D=deconvolution, R=relu, T=tanh. The numbers in parentheses indicate the number of filters, filter size, and stride of the convolution filters, respectively.

Encoder	Decoder	Discriminator
CL(64,4,2)	CBDR(256,4,1)	CBL(64,4,2)
CBL(128,4,2)	CBDR(128,4,2)	CBL(128,4,2)
CBL(256,4,2)	CBR(64,4,2)	CBL(256,4,2)
CBL(512,4,1)	CT(3,4,2)	CBL(512,4,2)
		C(1,3,1)

Table 2: Details of DRIBs in corresponding layers of Fig. 2. Acronyms: C=convolution, B=batch normalization, D=deconvolution, R=relu. The numbers in parentheses indicate the number of filters, filter size, stride, and dilation rate of the convolution filters, respectively.

Layer 1	Layer 2	Layer 3
CBR(256,1,1,1)	DBR(256,3,1,1)	
CBR(256,1,1,1)	DBR(256,3,1,2)	CB(512,1,1,1)
CBR(256,1,1,1)	DBR(256,3,1,3)	

The main features of DRIB architecture are as follows:

1. **Dilated convolutions:** Because of the loss of spatial information by subsampling (Yu et al., 2017), we reduce the number of stride-2 convolutions by replacing dilated convolu-

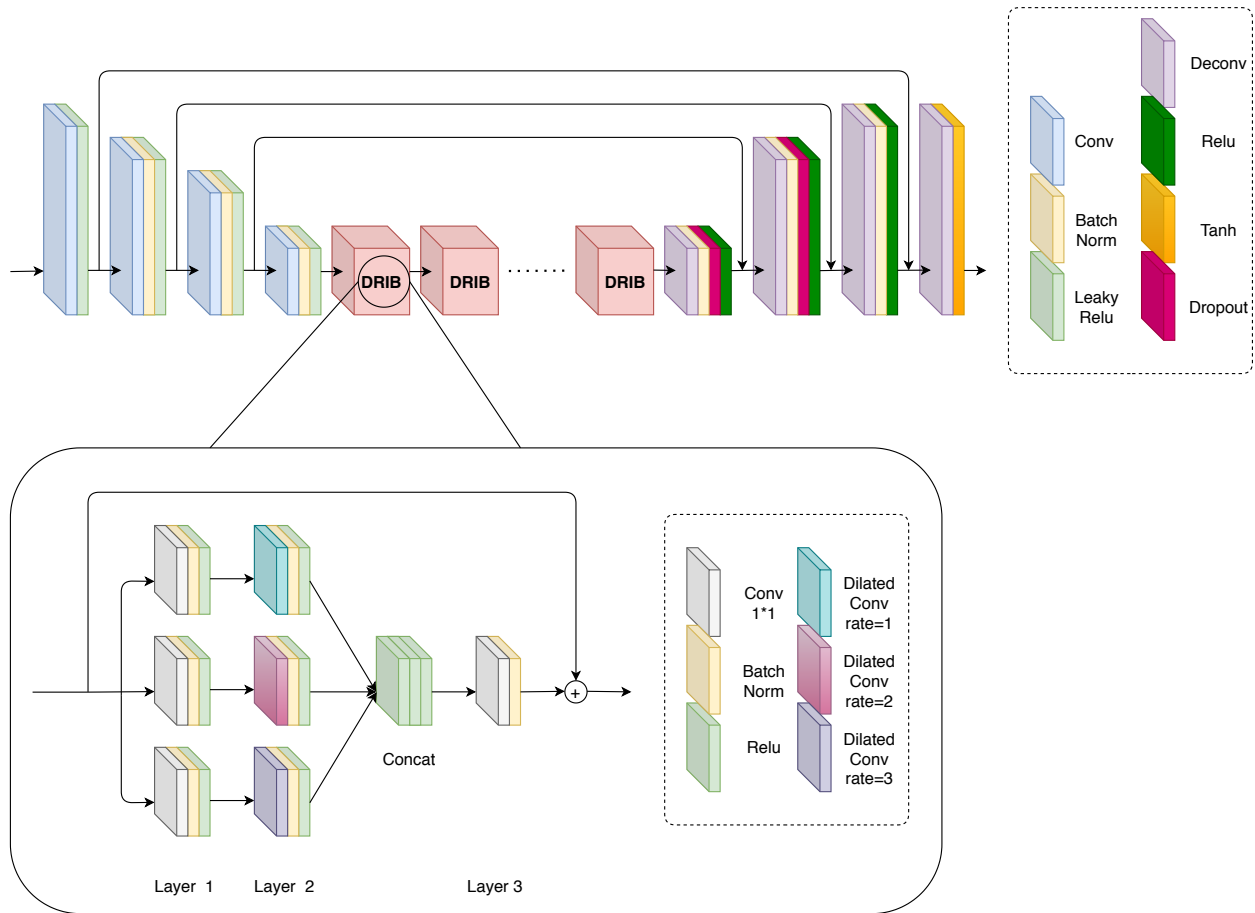


Figure 2: The architecture of the generator consists of an encoder, DRIBs, and decoder. A DRIB structure is magnified.

tions. Dilated convolutions prevent losing resolution by expanding the receptive field (Yu and Koltun, 2015), as shown in Fig. 3.

2. **Residual connections:** Learning becomes more difficult as networks deepen. The cause is the problem of vanishing/exploding gradients, which prevent the weights from changing their values. The residual connection is a way to tackle this problem (He et al., 2016).
3. **Inception modules:** We applied inception modules to process visual information at different scales (Szegedy et al., 2015). Also, it helped to reduce the depth of the network and allows for more efficient computations. Residual Inception Blocks were emerged by combining the inceptions modules and residual connections. This combination caused accelerating the training of inception networks (Szegedy et al., 2016).

Using these features for DRIBs halved the number of our generator parameters than U-net (Ronneberger et al., 2015) but raised performance.

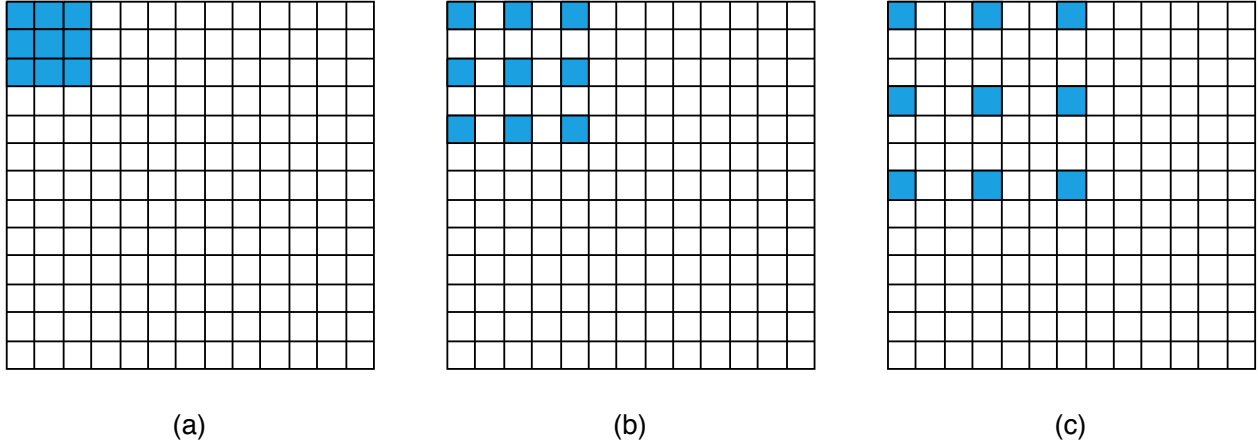


Figure 3: 3×3 Dilated convolutions with different dilation rate. (a) Dilated convolution, $r=1$. (b) Dilated convolution, $r=2$. (c) Dilated convolution, $r=3$. Dilated convolutions keep the spatial resolution by expanding the receptive field.

2.2. Objective

We used the objective of conditional GAN to both generator and discriminator networks, which can be expressed as:

$$L_{cGAN} = E_{x,y \sim p_{data}(x,y)}[\log(D(x,y))] + E_{x,z \sim p_{data}(x,z)}[\log(1 - D(x,G(x,z)))] \quad (1)$$

where D represents the discriminator network, G represents the generator network, and D tries to maximize the objective against an adversarial G that tries to minimize it.

To reduce blurring and bring the output image closer to the target image, we used L1 loss function as follows:

$$L_1 = \|G(x) - y\|_1 \quad (2)$$

where y represents the target image.

SSIM measures the similarity between two images and assesses quality based on the degradation of structural information (Wang et al., 2004). It is calculated between two images x and y as follows:

$$SSIM_{(x,y)} = \frac{(2\mu_x\mu_y + C_1)}{(\mu_x^2 + \mu_y^2 + C_1)} \cdot \frac{(2\sigma_{xy} + C_2)}{(\sigma_x^2 + \sigma_y^2 + C_2)} \quad (3)$$

where μ , σ^2 , and σ_{xy} are the average, variance, and covariance, respectively. C_1 and C_2 are variables to stabilize the division with weak denominator.

The SSIM loss function in patch P can be written as:

$$L_{ssim}(P) = \frac{1}{N} \sum (1 - SSIM_p) \quad (4)$$

where p is the center pixel of patch P . The size of the patch and Gaussian filter is 11×11 .

We added SSIM loss function to the pix2pix loss function to learn to produce visually delightful images (Zhao et al., 2016). The final objective of our generators is computed via:

$$L_G = L_{cGAN} + \lambda_1 L_1 + \lambda_2 L_{ssim} \quad (5)$$

where $\lambda_1 = 100$, $\lambda_2 = 100$.

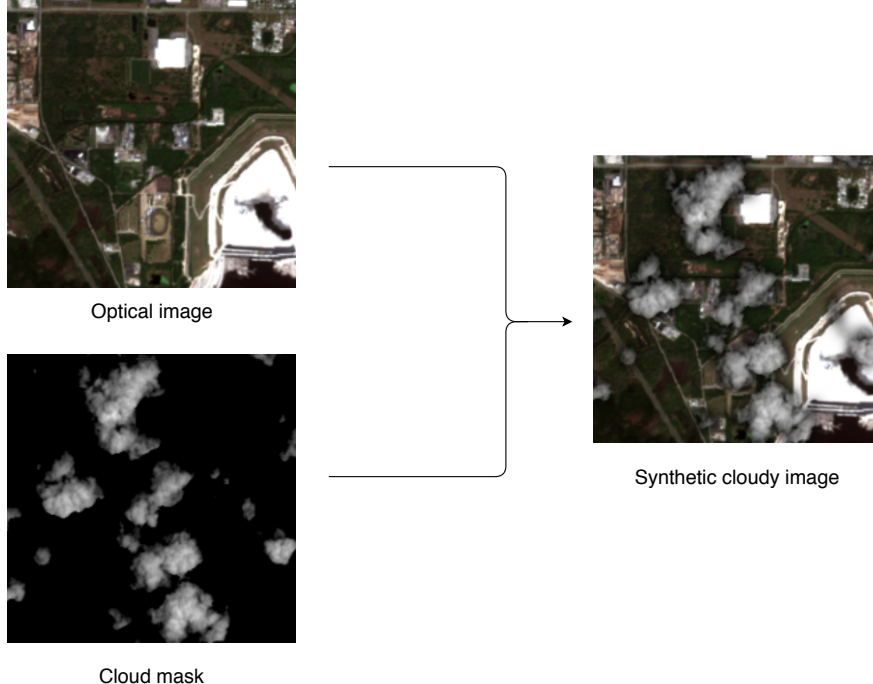


Figure 4: Alpha blending process

2.3. Training and testing

The GANs are trained with the SEN1-2 dataset (Schmitt et al., 2018) consisting of co-registered Sentinel-1 SAR and Sentinel-2 optical image patches with 256×256 px. Only VV and RGB bands were used for the dataset with a spatial sampling distance of 10m. All pixel values of images are normalized to $[-1, 1]$. We trained SAR-to-optical translation GAN with 18712 pair images and tested it with 4678.

For cloudy images, we used thick synthetic clouds that had been clipped from real cloudy images. Then cloud masks were added to optical images by alpha blending (Porter and Duff, 1984), as shown in Fig. 4. We eliminate background information from cloudy regions by this approach. Fig. 5 shows four examples of our dataset with different cloud percentages. We trained cloud removal GAN with 2000 pair images and tested it with 500.

3. Experimental results

In this section, we will first explain the details of the training. Then we demonstrate the evaluation metrics used, and we report the results of our comparisons based on them. Finally, we investigate the effect of DRIBs and SSIM loss function.

3.1. Implementation details

For both GANs, we set the following hyper-parameters: learning rate $\alpha = 2^{-4}$, batch size=32, dropout=0.5. We initialized the weights of the networks with normal distribution $\mathcal{N}(\mu = 0, \sigma^2 = 0.02)$. We used Adam optimizer with momentum parameters $\beta_1 = 0.5$ and $\beta_2 = 0.999$. The size of the inputs of the discriminator in SAR-to-optical translation GAN

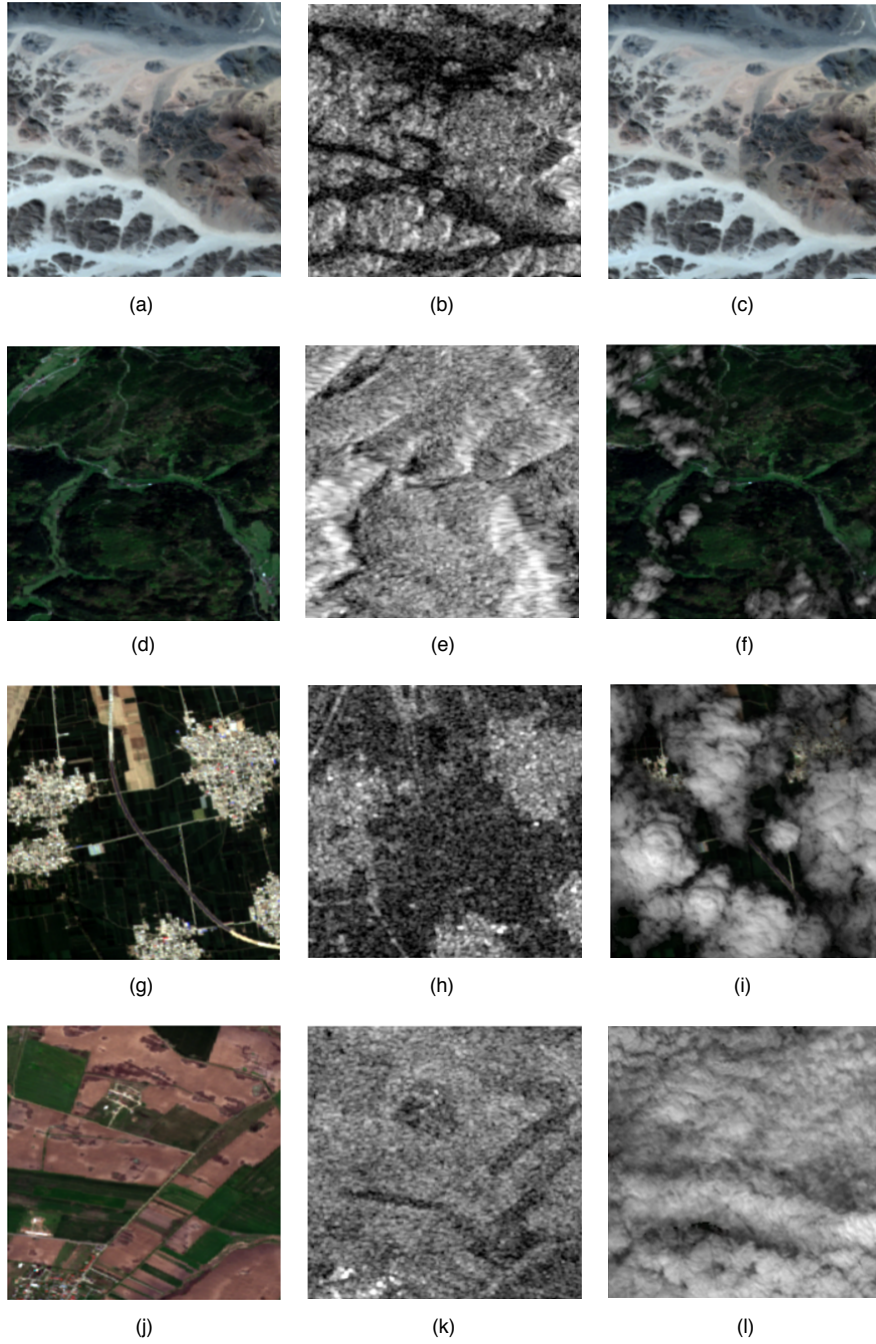


Figure 5: Examples of dataset; left: optical image, center: SAR image, right: cloudy image.

is set to $256 \times 256 \times 1$ and $256 \times 256 \times 3$. These sizes are $256 \times 256 \times 6$ and $256 \times 256 \times 3$ in cloud removal GAN.

3.2. Metrics

We evaluated our model in both SAR-to-optical translation and cloud removal parts with SSIM eq. 3 and peak signal to noise ratio (PSNR) as given by:

$$PSNR = 20 \cdot \log_{10}\left(\frac{MAX_I}{\sqrt{MSE}}\right) \quad (6)$$

where MAX_I represents the maximum possible pixel value of the image.

3.3. Performance comparison

This section compares the proposed method with state-of-the-art approaches in SAR-to-optical translation and cloud removal separately.

3.3.1. SAR-to-optical image translation

We compared our SAR-to-optical translation GAN with three deep learning-based models. (Bermudez et al., 2018; Enomoto et al., 2018; Li et al., 2020) used GANs with different architectures to translate SAR-to-optical images. The samples of generator outputs are presented in Fig. 6. Table 3 shows corresponding quantitative results.

Table 3: SAR to Opt translation performance comparison.

Method	PSNR	SSIM
(Bermudez et al., 2018)	17.1878	0.2981
(Enomoto et al., 2018)	18.6526	0.3606
(Li et al., 2020)	19.0713	0.4196
Ours	19.4495	0.4453

3.3.2. Cloud removal

To compare our cloud removal GAN, we use two GAN based methods, which used SAR and optical data fusion. (Grohnfeldt et al., 2018) presented a cGAN to remove clouds with SAR. Ebel et al. (2020) removed clouds using CycleGAN and auxiliary loss term. Fig. 7 presents cloudy images and corresponding cloud-free images generated by different methods. The PSNR and SSIM values are listed in Table 4. We measured PSNR for cloudy and non-cloudy areas separately to be able to assess the cloud removal power of models in cloudy areas accurately.

Table 4: Cloud removal performance comparison.

Method	PSNR	SSIM	PSNR (cloudy areas)	PSNR (non-cloudy areas)
(Ebel et al., 2020)	17.8966	0.4863	14.1949	21.9991
(Grohnfeldt et al., 2018)	19.2701	0.5535	15.9657	22.7272
Ours	23.0941	0.6909	19.9044	25.9061

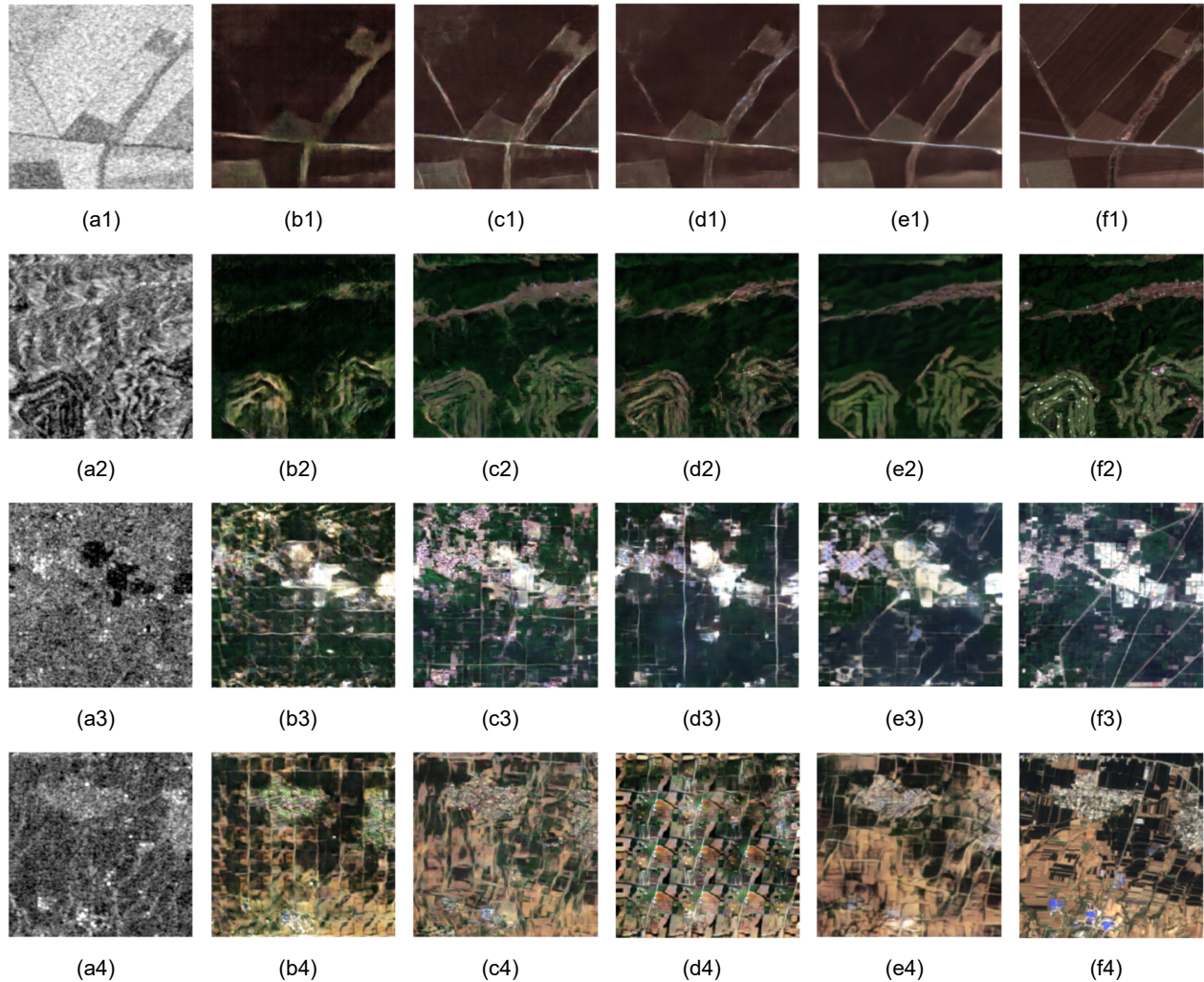


Figure 6: Example results of SAR to opt translation GAN. Column 1 shows SAR images, Column 2 results of (Bermudez et al., 2018) model, Column 3 results of (Enomoto et al., 2018) model, Column 4 results of (Li et al., 2020) model, Column 5 results of our model, and Column 6 target images.

3.4. Ablation study

3.4.1. Effect of SAR-to-optical image translation step and DRIBs

To prove the influence of the SAR-to-optical translation and DRIBs, we examined our model with different components for generators, as shown in Table 5. In the second row of Table 5, the SAR-to-optical translation is not used, and a cloud image with a SAR image are given to the input of the cloud removal generator. In the rest of the rows, we replaced DRIBs with U-net. The results show the effect of our model parts on improving the quality of output images.

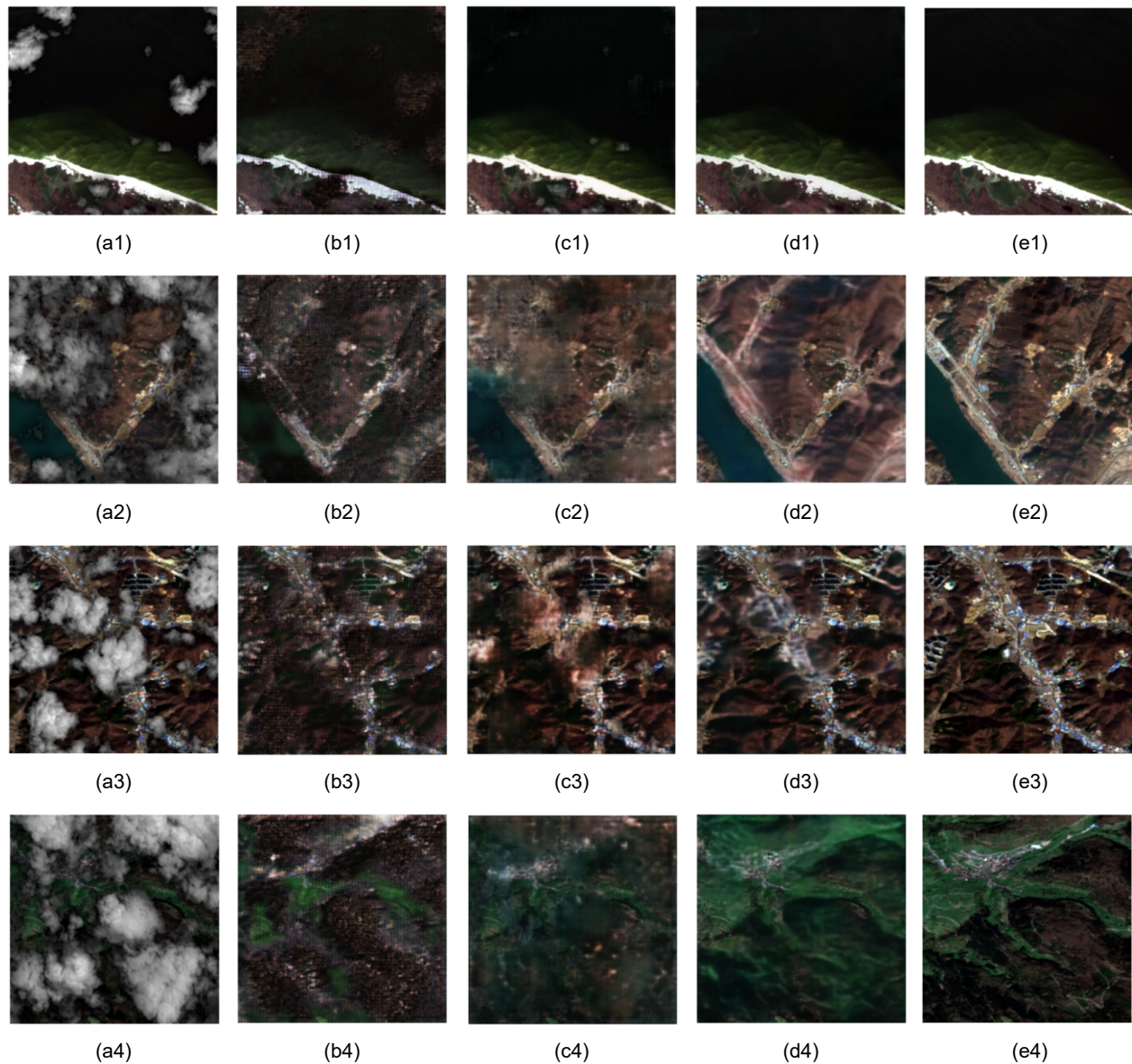


Figure 7: Example results of cloud removal GAN. Column 1 shows cloudy images, Column 2 results of (Ebel et al., 2020) model, Column 3 results of (Grohnfeldt et al., 2018) model, Column 4 results of our model, and Column 5 target images.

Table 5: Performance of our method when using different architectures for the generator.

Cloud Removal	SAR2OPT	PSNR	SSIM	PSNR (cloudy areas)	PSNR (non-cloudy areas)
DRIBs	-	16.5430	0.4515	15.4963	17.9218
U-NET	U-NET	21.3734	0.6150	19.7257	22.8087
DRIBs	U-NET	21.8911	0.6363	19.7043	23.8589
U-NET	DRIBs	22.6575	0.6835	19.8227	25.1819
DRIBs	DRIBs	23.0941	0.6909	19.9044	25.9061

3.4.2. Effect of SSIM loss function

In order to show the impact of the SSIM loss function, we abandoned it in different modes. Table 6 presents results of our investigation. PSNR and SSIM values increased by adding SSIM loss function.

Table 6: Performance of our method when using different loss functions.

Cloud Removal	SAR2OPT	PSNR	SSIM	PSNR (cloudy areas)	PSNR (non-cloudy areas)
L1	L1	20.4185	0.5304	18.6577	21.7619
SSIM+L1	L1	21.3423	0.6063	19.0759	23.0808
SSIM	SSIM	21.8548	0.6694	18.5796	24.7527
L1	SSIM+L1	22.0853	0.6309	19.4336	24.3254
SSIM+L1	SSIM+L1	23.0941	0.6909	19.9044	25.9061

4. Discussion

As the experimental results in Section 3 show, our model performs better than state-of-the-art methods. Tables 3 and 4 show that the proposed model has the highest PSNR and SSIM values in both SAR-to-optical translation and cloud removal parts. According to the PSNR values in cloudy and non-cloudy areas, it can be concluded that our model can remove the cloud very well and also keep the non-cloudy areas unchanged. This performance was due to using two GANs, changing the network structure, and adding the SSIM loss function. As explained in Section 2 about DRIB architecture, we expected better performance than classical U-net. Table 5 confirms DRIBs performance. Our results also showed that adding the SSIM loss function to the classical pix2pix loss function increased the PSNR and SSIM in the output images, as shown in Table 6.

5. Conclusions

In this paper, we proposed a model to remove clouds using two GANs and SAR images. Compared to previous GAN-based methods, our method has improvements in the two parts of the generator network structure and the loss function. The experimental results on the SEN1-2 dataset show the superiority of our model over the other state-of-the-art methods in both SAR-to-optical translation and cloud removal parts.

Developing a cloud removal model using real cloudy images and utilizing its generated images for classification tasks can be considered further. Providing a solution to remove the cloud from unpaired images can be another issue for future work.

Acknowledgment

This work was supported by the Center for Space Research of Iran.

References

- Benabdelkader, S., Melgani, F., Boulemden, M.. Cloud-contaminated image reconstruction with contextual spatio-spectral information. In: 2007 IEEE International Geoscience and Remote Sensing Symposium. IEEE; 2007. p. 373–376.
- Bermudez, J., Happ, P., Oliveira, D., Feitosa, R.. Sar to optical image synthesis for cloud removal with generative adversarial networks. *ISPRS Annals of Photogrammetry, Remote Sensing & Spatial Information Sciences* 2018;4(1).
- Bermudez, J.D., Happ, P.N., Feitosa, R.Q., Oliveira, D.A.. Synthesis of multispectral optical images from sar/optical multitemporal data using conditional generative adversarial networks. *IEEE Geoscience and Remote Sensing Letters* 2019;16(8):1220–1224.
- Chen, Y., Tang, L., Yang, X., Fan, R., Bilal, M., Li, Q.. Thick clouds removal from multitemporal zy-3 satellite images using deep learning. *IEEE Journal of Selected Topics in Applied Earth Observations and Remote Sensing* 2019;13:143–153.
- Cheng, Q., Shen, H., Zhang, L., Yuan, Q., Zeng, C.. Cloud removal for remotely sensed images by similar pixel replacement guided with a spatio-temporal mrf model. *ISPRS Journal of Photogrammetry and Remote Sensing* 2014;92:54–68.
- Ebel, P., Meraner, A., Schmitt, M., Zhu, X.X.. Multisensor data fusion for cloud removal in global and all-season sentinel-2 imagery. *IEEE Transactions on Geoscience and Remote Sensing* 2020;.
- Enomoto, K., Sakurada, K., Wang, W., Fukui, H., Matsuoka, M., Nakamura, R., Kawaguchi, N.. Filmy cloud removal on satellite imagery with multispectral conditional generative adversarial nets. In: *Proceedings of the IEEE Conference on Computer Vision and Pattern Recognition Workshops*. 2017. p. 48–56.
- Enomoto, K., Sakurada, K., Wang, W., Kawaguchi, N., Matsuoka, M., Nakamura, R.. Image translation between sar and optical imagery with generative adversarial nets. In: *IGARSS 2018-2018 IEEE International Geoscience and Remote Sensing Symposium*. IEEE; 2018. p. 1752–1755.
- Gao, J., Yuan, Q., Li, J., Zhang, H., Su, X.. Cloud removal with fusion of high resolution optical and sar images using generative adversarial networks. *Remote Sensing* 2020;12(1):191.
- Goodfellow, I., Pouget-Abadie, J., Mirza, M., Xu, B., Warde-Farley, D., Ozair, S., Courville, A., Bengio, Y.. Generative adversarial nets. In: *Advances in neural information processing systems*. 2014. p. 2672–2680.
- Grohnfeldt, C., Schmitt, M., Zhu, X.. A conditional generative adversarial network to fuse sar and multispectral optical data for cloud removal from sentinel-2 images. In: *IGARSS 2018-2018 IEEE International Geoscience and Remote Sensing Symposium*. IEEE; 2018. p. 1726–1729.

- He, K., Zhang, X., Ren, S., Sun, J.. Deep residual learning for image recognition. In: Proceedings of the IEEE conference on computer vision and pattern recognition. 2016. p. 770–778.
- Isola, P., Zhu, J.Y., Zhou, T., Efros, A.A.. Image-to-image translation with conditional adversarial networks. In: Proceedings of the IEEE conference on computer vision and pattern recognition. 2017. p. 1125–1134.
- King, M.D., Platnick, S., Menzel, W.P., Ackerman, S.A., Hubanks, P.A.. Spatial and temporal distribution of clouds observed by modis onboard the terra and aqua satellites. *IEEE Transactions on Geoscience and Remote Sensing* 2013;51(7):3826–3852.
- Kussul, N., Lavreniuk, M., Skakun, S., Shelestov, A.. Deep learning classification of land cover and crop types using remote sensing data. *IEEE Geoscience and Remote Sensing Letters* 2017;14(5):778–782.
- LeCun, Y., Bengio, Y., Hinton, G.. Deep learning. *nature* 2015;521(7553):436–444.
- Li, W., Li, Y., Chan, J.C.W.. Thick cloud removal with optical and sar imagery via convolutional-mapping-deconvolutional network. *IEEE Transactions on Geoscience and Remote Sensing* 2019;58(4):2865–2879.
- Li, Y., Fu, R., Meng, X., Jin, W., Shao, F.. A sar-to-optical image translation method based on conditional generation adversarial network (cgan). *IEEE Access* 2020;8:60338–60343.
- Lyu, H., Lu, H., Mou, L.. Learning a transferable change rule from a recurrent neural network for land cover change detection. *Remote Sensing* 2016;8(6):506.
- Ma, L., Liu, Y., Zhang, X., Ye, Y., Yin, G., Johnson, B.A.. Deep learning in remote sensing applications: A meta-analysis and review. *ISPRS journal of photogrammetry and remote sensing* 2019;152:166–177.
- Maalouf, A., Carré, P., Augereau, B., Fernandez-Maloigne, C.. A bandelet-based inpainting technique for clouds removal from remotely sensed images. *IEEE transactions on geoscience and remote sensing* 2009;47(7):2363–2371.
- Meng, F., Yang, X., Zhou, C., Li, Z.. A sparse dictionary learning-based adaptive patch inpainting method for thick clouds removal from high-spatial resolution remote sensing imagery. *Sensors* 2017;17(9):2130.
- Meraner, A., Ebel, P., Zhu, X.X., Schmitt, M.. Cloud removal in sentinel-2 imagery using a deep residual neural network and sar-optical data fusion. *ISPRS Journal of Photogrammetry and Remote Sensing* 2020;166:333–346.
- Mirza, M., Osindero, S.. Conditional generative adversarial nets. arXiv preprint arXiv:14111784 2014;.
- Porter, T., Duff, T.. Compositing digital images. In: Proceedings of the 11th annual conference on Computer graphics and interactive techniques. 1984. p. 253–259.

- Ronneberger, O., Fischer, P., Brox, T.. U-net: Convolutional networks for biomedical image segmentation. In: International Conference on Medical image computing and computer-assisted intervention. Springer; 2015. p. 234–241.
- Schmitt, M., Hughes, L.H., Zhu, X.X.. The sen1-2 dataset for deep learning in sar-optical data fusion. arXiv preprint arXiv:180701569 2018;.
- Shen, H., Li, X., Cheng, Q., Zeng, C., Yang, G., Li, H., Zhang, L.. Missing information reconstruction of remote sensing data: A technical review. *IEEE Geoscience and Remote Sensing Magazine* 2015;3(3):61–85.
- Singh, P., Komodakis, N.. Cloud-gan: Cloud removal for sentinel-2 imagery using a cyclic consistent generative adversarial networks. In: IGARSS 2018-2018 IEEE International Geoscience and Remote Sensing Symposium. IEEE; 2018. p. 1772–1775.
- Szegedy, C., Ioffe, S., Vanhoucke, V., Alemi, A.. Inception-v4, inception-resnet and the impact of residual connections on learning. arXiv preprint arXiv:160207261 2016;.
- Szegedy, C., Liu, W., Jia, Y., Sermanet, P., Reed, S., Anguelov, D., Erhan, D., Vanhoucke, V., Rabinovich, A.. Going deeper with convolutions. In: Proceedings of the IEEE conference on computer vision and pattern recognition. 2015. p. 1–9.
- Vakalopoulou, M., Karantzas, K., Komodakis, N., Paragios, N.. Building detection in very high resolution multispectral data with deep learning features. In: 2015 IEEE International Geoscience and Remote Sensing Symposium (IGARSS). IEEE; 2015. p. 1873–1876.
- Wang, L., Xu, X., Yu, Y., Yang, R., Gui, R., Xu, Z., Pu, F.. Sar-to-optical image translation using supervised cycle-consistent adversarial networks. *IEEE Access* 2019;7:129136–129149.
- Wang, Z., Bovik, A.C., Sheikh, H.R., Simoncelli, E.P.. Image quality assessment: from error visibility to structural similarity. *IEEE transactions on image processing* 2004;13(4):600–612.
- Wang, Z., Jin, J., Liang, J., Yan, K., Peng, Q.. A new cloud removal algorithm for multispectral images. In: MIPPR 2005: SAR and Multispectral Image Processing. International Society for Optics and Photonics; volume 6043; 2005. p. 60430W.
- Xu, M., Jia, X., Pickering, M., Plaza, A.J.. Cloud removal based on sparse representation via multitemporal dictionary learning. *IEEE Transactions on Geoscience and Remote Sensing* 2016;54(5):2998–3006.
- Yu, F., Koltun, V.. Multi-scale context aggregation by dilated convolutions. arXiv preprint arXiv:151107122 2015;.
- Yu, F., Koltun, V., Funkhouser, T.. Dilated residual networks. In: Proceedings of the IEEE conference on computer vision and pattern recognition. 2017. p. 472–480.

- Zhang, L., Zhang, M., Sun, X., Wang, L., Cen, Y.. Cloud removal for hyperspectral remotely sensed images based on hyperspectral information fusion. *International Journal of Remote Sensing* 2018;39(20):6646–6656.
- Zhang, Q., Yuan, Q., Li, J., Li, Z., Shen, H., Zhang, L.. Thick cloud and cloud shadow removal in multitemporal imagery using progressively spatio-temporal patch group deep learning. *ISPRS Journal of Photogrammetry and Remote Sensing* 2020;162:148–160.
- Zhao, H., Gallo, O., Frosio, I., Kautz, J.. Loss functions for image restoration with neural networks. *IEEE Transactions on computational imaging* 2016;3(1):47–57.
- Zhu, J.Y., Park, T., Isola, P., Efros, A.A.. Unpaired image-to-image translation using cycle-consistent adversarial networks. In: *Proceedings of the IEEE international conference on computer vision*. 2017. p. 2223–2232.